SIAM J. CONTROL OPTIM.
Vol. 63, No. 4, pp. 2451–2471

TOPOGRAPHY OPTIMIZATION FOR ENHANCING MICROALGAL GROWTH IN RACEWAY PONDS*

OLIVIER BERNARD†, LIU-DI LU‡, JACQUES SAINTE-MARIE§, AND JULIEN SALOMON§

Abstract. Modeling the evolution process for the growth of microalgae in an artificial pond is a huge challenge given the complex interaction between hydrodynamics and biological processes occurring across various timescales. In this paper, we consider a raceway, i.e., an oval pond where the water is set in motion by a paddle wheel. Our aim is to investigate theoretically and numerically the impact of bottom topography in such raceway ponds on microalgae growth. To achieve this goal, we consider a biological model based on the Han model, coupled with the Saint-Venant systems that model the fluid. We then formulate an optimization problem for which we apply the weak maximum principle to characterize optimal topographies that maximize biomass production over one lap of the raceway pond or multiple laps with a paddle wheel. In contrast to a widespread belief in the field of microalgae, we show that a flat topography in a periodic regime satisfies the necessary optimality condition and observe in the numerical experiments that the flat topography is actually optimal in this case. However, nontrivial topographies may be more advantageous in alternative scenarios, such as when considering the effects of mixing devices within the model. This study sheds light on the intricate relationship between bottom topography, fluid dynamics, and microalgae growth in raceway ponds, offering valuable insights into optimizing biomass production.

Key words. optimal control, weak maximum principle, microalgae, Han model, Saint-Venant system, raceway pond, shape optimization

MSC codes. 35Q93, 65K10, 76B75, 92B25

DOI. 10.1137/23M1616297

1. Introduction.

The numerical design of microalgae production technologies has been for decades a source of many interesting challenges not only in engineering but also in the area of scientific computing [13, 24, 38, 21]. The potential of these emerging photosynthetic organisms is found in cosmetics, pharmaceutical fields, food, and, in the long term, green chemistry and energy applications [37]. Outdoor production is mainly carried out in open bioreactors with a raceway shape. Algae grow while exposed to solar radiation in these circular basins, where the water is set in motion by a paddle wheel. This mixing device homogenizes the medium, ensures equidistribution of nutrients, and guarantees that each cell will have regular access to light [9, 12]. The algae are harvested periodically, and their concentration is maintained around an optimal value [28, 31]. The penetration of light is strongly reduced by the algal biomass, and less than 1% of the incident light reaches the reactor bottom [6]. In the case of larger biomass, the light extinction is so high that a large fraction of the population evolves in the dark and does not grow anymore. At low biomass density, a fraction of the solar light is not used by the algae, and the productivity is suboptimal.

*Received by the editors November 12, 2023; accepted for publication (in revised form) April 17, 2025; published electronically July 15, 2025.
https://doi.org/10.1137/23M1616297

†Inria Centre Université Côte d'Azur, GreenOwl, 06902 Sophia-Antipolis Cedex, France, and Sorbonne Université, INSU-CNRS, Laboratoire d'Océanographie de Villefranche, 06230 Villefranche-sur-mer, France (olivier.bernard@inria.fr).
‡Section de Mathématiques, Université de Genéve, 1205 Geneva, Switzerland (liudi.lu@unige.ch).
§Sorbonne Université, Université Paris Cité, CNRS, INRIA, Laboratoire Jacques-Louis Lions, LJLL, EPC ANGE, F-75005 Paris, France (jacques.sainte-marie@inria.fr, julien.salomon@inria.fr).

Theoretical work has determined the optimal biomass for maximizing productivity [23, 17, 2].

Here, we consider another approach which consists in improving the photoproduction process by controlling the cell trajectories in the light field. We start from the observation that algal raceway ponds are dynamical systems combining a physical aspect—the hydrodynamic behavior of the fluid transporting the algae culture—and a biological aspect—the light harvesting by chlorophyll complexes in the cells [1, 29, 30]. We then study the effect of topography (or bathymetry) on growth to optimize the light received by the microalgae. Modeling this system is challenging since it also involves the free-surface incompressible Navier–Stokes system [7, 10, 36, 27]. The complexity of this model generally prevents obtaining explicit formulas, and large computational resources are required to perform simulations.

Several experimental campaigns [25, 32] have shown that in straight sections of the raceway, the flow is not disturbed (which was further confirmed by CFD modeling [19, 20]). Therefore, in these regions, despite turbulent dispersion, mixing is relatively poor. This mixing is mainly induced locally by the paddle wheel and, to a lesser extent, by the bends. The recent study of [20] confirms this finding; i.e., the turbulence is mainly generated near the paddle wheel and close to the surface.

We therefore focus on the main part of the raceway, outside the paddle-wheel area, and assume laminar flux. We study how to improve productivity in this part by modifying the bottom topography. This enables us to discuss the common belief that some specific topographies can bring more light to the algae in lower parts of the raceway since cells get closer to the surface when reaching peaks in these topographies.

Let us detail our approach. We first introduce a coupled model to represent the growth of algae in a one-dimensional raceway pond, accounting for the light that they receive. This model is obtained by combining the Han photosynthesis equations with a hydrodynamic law based on the Saint-Venant system. This first step enables us to formulate an optimization problem in which the topography of the raceway is designed to maximize productivity. We then use an adjoint-based optimization scheme to include the constraints associated with the Saint-Venant regime. We prove that the flat topography satisfies the first-order optimality systems in a periodic case, focusing on the fraction of the raceway in a laminar regime. However, nontrivial topographies can be obtained in other contexts, e.g., when the periodic assumption is removed or when the mixing device is accounted for in conjunction with the bottom topography. Numerical simulations show that a combination of turbulence-induced mixing and nonflat topographies can slightly increase biomass production. However, enhancing the turbulence by mixing significantly increases productivity and is definitely the most efficient approach [5, 4] even if more energy is dissipated in this process.

The outline of the paper is as follows. In section 2, we present the biological and hydrodynamic models underlying our coupled system. In section 3, we describe the optimization problem and a corresponding numerical optimization procedure. Section 4 is devoted to the numerical results obtained with our approach. We then conclude with some perspectives opened up by this work.

2. Hydrodynamic and biological models. Our approach is based on a coupling of the hydrodynamic transport of the particles with the photosystem evolution driven by the light intensity they receive when traveling in the raceway pond.

2.1. Hydrodynamic model and Lagrangian trajectories. Saint-Venant equations are a popular model of geophysical flows. This system is derived from the free surface incompressible Navier–Stokes equations (see, for instance, [15]). Here, we

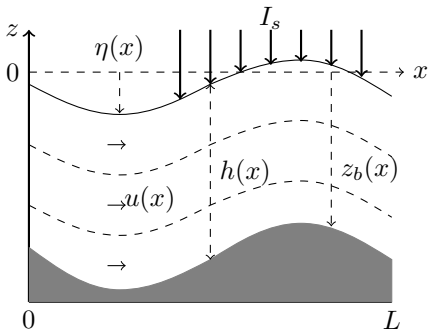

FIG. 2.1. *Representation of the one-dimensional hydrodynamic model.*

focus on its one-dimensional smooth steady-state solutions in a laminar regime, which satisfy

$$\partial_x(hu) = 0, \quad \partial_x\left(hu^2 + g\frac{h^2}{2}\right) = -gh\partial_x z_b, \tag{2.1}$$

where h is the water depth, u is the horizontal averaged velocity of the fluid, g is the gravitational constant, and z_b is the topography. The free surface η and the average discharge are given by $\eta := h + z_b$ and $Q = hu$, respectively. This system is presented in Figure 2.1. The z-axis (resp., x-axis) represents the vertical (resp., horizontal) direction, and I_s is the light intensity on the free surface (assumed to be constant).

Integrating the equation on the left of (2.1), we get

$$hu = Q_0 \tag{2.2}$$

for a fixed positive constant Q_0. This implies a constant discharge in space. Then the equation on the right-hand side of (2.1) can be rewritten by

$$hu\partial_x u + h\partial_x gh + h\partial_x g z_b = 0. \tag{2.3}$$

Assume that h is nonzero. Dividing then the equality (2.3) by h and using (2.2) to eliminate u, we get $\partial_x(\frac{Q_0^2}{2h^2} + g(h + z_b)) = 0$. Given $h(0), z_b(0) \in \mathbb{R}$, we obtain

$$\frac{Q_0^2}{2h(x)^2} + g(h(x) + z_b(x)) = \frac{Q_0^2}{2h^2(0)} + g(h(0) + z_b(0)) =: M_0,$$

which holds for all $x \in [0, L]$, meaning that the topography z_b satisfies

$$z_b = \frac{M_0}{g} - \frac{Q_0^2}{2gh^2} - h. \tag{2.4}$$

Remark 2.1. Let $Fr = \frac{u}{\sqrt{gh}}$ be the Froude number. The situation $Fr < 1$ corresponds to the subcritical case (i.e., the flow regime is *fluvial*), while $Fr > 1$ corresponds to the supercritical case (i.e., the flow regime is *torrential*). In the steady case, the threshold value $h = h_c$ is obtained for $Fr = 1$; using (2.2), we find $h_c := (\frac{Q_0^2}{g})^{\frac{1}{3}}$.

Because of (2.4), h solves a third-order polynomial equation. Given a smooth topography z_b, if $h_c + z_b + \frac{Q_0^2}{2gh_c^2} - \frac{M_0}{g} < 0$, then there exists a unique positive smooth solution of (2.4) that satisfies the subcritical flow condition (see [26, Lemma 1]).

From the incompressibility of the flow, we have $\nabla \cdot \underline{\mathbf{u}} = 0$ with $\underline{\mathbf{u}} = (u(x), w(x,z))$. Here, $w(x,z)$ is the vertical velocity. Incompressibility implies that $\partial_x u + \partial_z w = 0$. Integrating the latter from the topography z_b to an arbitrary vertical position z gives

$$\begin{aligned} 0 &= \int_{z_b}^{z} \big(\partial_x u(x) + \partial_\xi w(x,\xi)\big) \mathrm{d}\xi \\ &= (z - z_b)\partial_x u(x) + w(x,z) - w(x,z_b) \\ &= (z - z_b)\partial_x u(x) - u(x)\partial_x z_b + w(x,z) \\ &= \partial_x\big((z - z_b)u(x)\big) + w(x,z), \end{aligned}$$

where we have used the kinematic condition at the bottom, i.e., $w(x,z_b) = u(x)\partial_x z_b$. It follows from (2.4) that

$$w(x,z) = \left(\frac{M_0}{g} - \frac{3u^2(x)}{2g} - z\right) u'(x), \tag{2.5}$$

with $u'(x)$ the derivative of u with respect to x.

Let the pair $(x(t), z(t))$ be the position of a particle (or an algal cell) at time t in the raceway pond. The Lagrangian trajectory is characterized by

$$\begin{pmatrix} \dot{x}(t) \\ \dot{z}(t) \end{pmatrix} = \begin{pmatrix} u(x(t)) \\ w\big(x(t), z(t)\big) \end{pmatrix}, \tag{2.6}$$

with the initial position at time $t = 0$, $(x(0), z(0)) = (x_0, z_0)$.

Remark 2.2. The geometry of the raceway pond with small dissipation and shear effects (reduced wall friction and viscosity) justifies a laminar flow modeled by a shallow-water model, such as the Saint-Venant system. This regime also minimizes the mixing energy and hence is favored at the industrial scale.

A higher mixing energy would lead to a turbulent regime. A possible way to enrich the representation of Lagrangian trajectories in this case would consist of including a Brownian in (2.6). However, getting time-free expressions of the trajectories (as in (2.7) and (2.12)) in this case is much more challenging, as such a strategy would require a large set of simulations together with an averaging strategy.

The Lagrangian trajectory given by (2.6) is a general formulation which still holds when we change the hydrodynamic model. In our setting, we can find a time-free formulation of the Lagrangian trajectory. More precisely, we denote by $z(x)$ the depth of a particle at position x. From (2.5) and (2.6), we get

$$z' := \frac{\dot{z}}{\dot{x}} = \left(\frac{M_0}{g} - \frac{3u^2}{2g} - z\right) \frac{u'}{u}. \tag{2.7}$$

From (2.2) and (2.4) and the definition of the free surface η, we have

$$\eta = h + z_b = \frac{M_0}{g} - \frac{u^2}{2g},$$

which implies that $\eta' = -uu'/g$. Multiplying then (2.7) on both sides by u and using the formulation of η and η', one finds

$$z'u + zu' = \left(\eta - \frac{u^2}{g}\right) u' = \eta u' + \eta' u,$$

which implies that $(u(z-\eta))' = 0$. Using again the identity (2.2), one obtains $\eta(x) - z(x) = \frac{h(x)}{h(0)}\big(\eta(0) - z(0)\big)$. This equation shows that given the initial water depth $h(0)$ and the initial free surface position $\eta(0)$, the distance between a trajectory z (starting from the position $z(0)$) and the free surface η depends only on the water depth h. On the other hand, the time-free formulation of the trajectory reads as

$$z(x) = \eta(x) - \frac{h(x)}{h(0)}\big(\eta(0) - z(0)\big). \tag{2.8}$$

We will further exploit the property of this formulation in section 3.

Remark 2.3. Since Q_0 is chosen to be positive, h is necessarily positive. Moreover, if $z(0)$ belongs to $[z_b(0), \eta(0)]$, then $z(x)$ belongs to $[z_b(x), \eta(x)]$. In particular, choosing $z(0) = z_b(0)$ in (2.8) and using (2.2) gives $z(x) = z_b(x)$. In the same way, we find that $z(x) = \eta(x)$ when $z(0) = \eta(0)$.

2.2. Modeling the dynamics of the photosystems. To describe the dynamics of photosystems, we use here the Han model [18]. This model is generally considered to characterize the photosynthetic process of these subunits as they harvest photons and transfer their energy to the cell to fix CO_2.

2.2.1. The Han model. The Han model is a compartmental model in which the photosystems are described by three different states: open and ready to harvest a photon (A), closed while processing the absorbed photon energy (B), or inhibited if several photons have been absorbed simultaneously (C). The relation of these three states are schematically presented in Figure 2.2.

The evolution satisfies the following ODEs:

$$\begin{aligned} \dot{A} &= -\sigma I A + \frac{B}{\tau}, \\ \dot{B} &= \sigma I A - \frac{B}{\tau} + k_r C - k_d \sigma I B, \\ \dot{C} &= -k_r C + k_d \sigma I B. \end{aligned} \tag{2.9}$$

Here, I denotes the light density, a continuous time-varying signal. The states A, B, and C are the relative frequencies of the three possible states with $A + B + C = 1$ so that (2.9) can be reduced to a system in dimension two by eliminating the state B. Here, σ stands for the specific photon absorption, τ is the turnover rate, and k_r and k_d represent the photosystem repair and damage rates, which are all positive.

The dynamics of the open state A can be shown to be much faster than the dynamics of the photoinhibition state C. A slow-fast approximation by using singular perturbation theory (as shown in details in [21]) leads to the simplification of the dynamics driven by the slow dynamics of C,

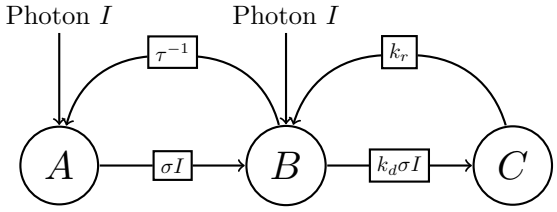

FIG. 2.2. *The Han model, describing the state transition probability, as a function of the photon flux.*

$$\dot{C} = -\alpha(I)C + \beta(I), \tag{2.10}$$

where

$$\alpha(I) = k_d\tau\frac{(\sigma I)^2}{\tau\sigma I + 1} + k_r, \quad \beta(I) = k_d\tau\frac{(\sigma I)^2}{\tau\sigma I + 1}. \tag{2.11}$$

Repeating the reasoning done to get (2.7) with (2.10) and (2.2), we can also find a time-free reformulation, namely,

$$C' := \frac{\dot{C}}{\dot{x}} = \frac{-\alpha(I)C + \beta(I)}{Q_0}h, \tag{2.12}$$

where all the functions on the right-hand side only depend on the spatial variable x.

2.2.2. Periodic setting. We consider the case where C is periodic, with a period corresponding to one lap of the raceway pond. This situation occurs, e.g., when an appropriate harvest is performed after each lap. To describe the corresponding model, we first consider a variant of the usual Cauchy problem (2.12):

Given $I \in \mathcal{C}([0,L];\mathbb{R})$, $I \geq 0$, find $(C_0, C) \in [0,1] \times \mathcal{C}([0,L];[0,1])$ such that

$$\begin{cases} C'(x) = \dfrac{-\alpha\big(I(x)\big)C(x) + \beta\big(I(x)\big)}{Q_0}h(x), \quad x \in [0,L], \\ C(L) = C(0) = C_0. \end{cases} \tag{2.13}$$

Let us show that the solution $C(x)$ of (2.13) exists. Indeed, applying Duhamel's formula to the Cauchy problem associated with (2.12) and the initial condition $C(0) = C_0$ and using the inequality $\beta(I) \leq \alpha(I)$ gives

$$\begin{aligned} C(L) - C_0 &= -\left(1 - e^{-\int_0^L \frac{\alpha(I(s))h(s)}{Q_0}\,\mathrm{d}s}\right)C_0 + \int_0^L e^{-\int_s^L \frac{\alpha(I(y))h(y)}{Q_0}\,\mathrm{d}y}\frac{\beta\big(I(s)\big)h(s)}{Q_0}\,\mathrm{d}s \\ &\leq \left(1 - e^{-\int_0^L \frac{\alpha(I(s))h(s)}{Q_0}\,\mathrm{d}s}\right)(1 - C_0)\,. \end{aligned}$$

Hence, the affine mapping $\Phi : C_0 \mapsto C(L) - C_0$ satisfies $\Phi(0) \geq 0$, and the inequality implies that $\Phi(1) \leq 0$. It follows that there exists a unique $C_0 \in [0,1]$ that satisfies $C(L) - C_0 = 0$. Using the *intermediate value theorem,* we get the next result.

THEOREM 2.4. *There exists a unique couple $(C_0, C) \in [0,1] \times \mathcal{C}([0,L];[0,1])$ that satisfies* (2.13).

2.2.3. Growth rate. Finally, the net growth rate of the photosystem is defined by balancing photosynthesis and respiration, which gives

$$\mu(C, I) := \zeta(I) - \gamma(I)C, \tag{2.14}$$

where

$$\gamma(I) = \frac{k\sigma I}{\tau\sigma I + 1}, \quad \zeta(I) = \frac{k\sigma I}{\tau\sigma I + 1} - R. \tag{2.15}$$

Here, k is a factor that relates the received energy with the growth rate, and R represents the respiration rate.

2.3. Coupling of two systems. As shown in the previous section, the light intensity I plays an important role in algal growth since it triggers photosynthesis. On the other hand, the position of the algae influences the perceived light as well as the efficiency of the photosynthesis process. Therefore, light intensity is the main connection that couples the hydrodynamic model and the physiological evolution of algae. To evaluate the light intensity observed on the trajectory z, we assume that the growth process occurs at a much slower timescale than that of hydrodynamics and is, as such, negligible for one lap over the raceway. In the same way, uncertainties such as rainfall and evaporation can also be neglected at this timescale. These factors can be taken into account for longer timescale using more detailed models; see, for instance, [11, 8]. In this framework, the Beer–Lambert law describes how light is attenuated with depth ξ by $I(x,\xi) := I_s \exp\big(-\varepsilon(\eta(x)-\xi)\big)$, where ε is the light extinction coefficient. Replacing ξ in the previous formulation by the trajectory (2.8), we then get the following expression for the captured light intensity along the trajectory $z(x)$:

$$I\big(x,z(x)\big) = I_s \exp\left(-\varepsilon \frac{h(x)}{h(0)}\big(\eta(0)-z(0)\big)\right). \tag{2.16}$$

In particular, we observe that for given data I_s, ε, $h(0)$, and $\eta(0)$, the perceived light intensity along the trajectory $z(x)$ depends only on its initial position $z(0)$ and $h(x)$.

In order to evaluate the quality of this coupled system, we define the average net growth rate of the system by

$$\bar{\mu} := \frac{1}{V}\int_0^L \int_{z_b(x)}^{\eta(x)} \mu\big(C(x,z), I(x,z)\big)\,\mathrm{d}z\mathrm{d}x, \tag{2.17}$$

where μ is defined by (2.14) and $V := \int_0^L h(x)\mathrm{d}x$ is the volume of our one-dimensional raceway.

3. Optimal control problem. In this section, we define the optimal control problems associated with our biological-hydrodynamic model. Depending on V, we divide our study into two cases.

3.1. Objective function and vertical discretization. Our goal is to find the optimal topography z_b that maximizes the average net growth rate (2.17). In order to tackle numerically this optimization problem, let us first consider a vertical discretization. Let N_z denotes the number of trajectories. We consider a uniform vertical discretization of their initial position:

$$z_i(0) := \eta(0) - \frac{i-\frac{1}{2}}{N_z} h(0), \quad i = 1,\dots,N_z. \tag{3.1}$$

Using the formulation (2.8), we find the trajectories $z_i(x) := \eta(x) - \frac{i-\frac{1}{2}}{N_z}h(x)$, $i = 1,\dots,N_z$. In particular, the distribution of the trajectories $z_i(x)$ remains uniform along the direction of x. Using (3.1), we obtain the perceived light intensity on $z_i(x)$,

$$I\big(x,z_i(x)\big) = I_s \exp\left(-\varepsilon \frac{h(x)}{h(0)}\big(\eta(0)-z_i(0)\big)\right) = I_s \exp\left(-\varepsilon \frac{i-\frac{1}{2}}{N_z} h(x)\right), \tag{3.2}$$

where we use the closed form of the light intensity (2.16) and the definition of $z_i(0)$. To simplify the notation and emphasize the dependence on the water depth h,

we write $I_i(h(x))$ instead of $I(x, z_i(x))$ hereafter. The photoinhibition state C_i is then computed using the evolution (2.12) for $I = I_i(h)$. In this setting, the semidiscrete average net growth rate in the raceway pond can be derived from (2.17) as

$$\bar{\mu}_{N_z}(h) := \frac{1}{VN_z} \sum_{i=1}^{N_z} \int_0^L \mu\Big(C_i(x), I_i\big(h(x)\big)\Big) h(x)\, \mathrm{d}x, \tag{3.3}$$

where h is the variable of the objective function and μ is given by (2.14). From now on, we focus on the subcritical case, i.e., $Fr < 1$ (see Remark 2.1). As mentioned in section 2.1, in this regime, a given topography z_b corresponds to a unique water depth h, which verifies this assumption.

Remark 3.1. Given a topography z_b, the usual shallow-water solvers typically consider equations of type (2.4) to compute h in the simulations. Here, we use this equation in the opposite way, i.e., to recover z_b from h. In this way, we directly optimize h instead of z_b since the expressions of the evolution of the state C (2.12), the light intensity (3.2), and the objective function (3.3) depend on h and not on z_b.

3.2. Constant volume. For simplicity, we omit from now on the variable x in the notation and consider h as the variable of the light intensities $(I_i)_{i=1,\dots,N_z}$ and $\bar{\mu}_{N_z}$. For a fixed volume $V > 0$ and a discharge $Q_0 > 0$, we seek admissible controls $h \in L^\infty([0, L]; \mathbb{R})$, $h > 0$, over a fixed length $L > 0$, which maximize the semidiscrete average net growth rate (3.3). Thus, the optimal control problem reads as

$$\begin{aligned}
\max_{h \in L^\infty([0,L];\,\mathbb{R}),\ h>0} \bar{\mu}_{N_z}(h) = & \sum_{i=1}^{N_z} \int_0^L \frac{\mu\Big(C_i(x), I_i\big(h(x)\big)\Big)}{VN_z} h(x)\, \mathrm{d}x \\
\text{s.t.} \quad C_i' = & \frac{\beta\left(I_i(h)\right) - \alpha\left(I_i(h)\right) C_i}{Q_0} h, \\
C_i(0) = & \, C_i(L) \qquad \forall i = 1, \cdots, N_z, \\
v' = & \, h, \\
v(0) = 0, & \ v(L) = V.
\end{aligned} \tag{P1}$$

Here, we use formula (2.14) for μ, h is the control variable, and (C_i, v) are the state variables, where v has been introduced to take into account the constraint $V = hL$. The Hamiltonian associated with (P1) is given by

$$\begin{aligned}
H(C_i, v, p_{C_i}, p_v, p_0, h) = & \sum_{i=1}^{N_z} p_{C_i} \frac{\beta\left(I_i(h)\right) - \alpha\left(I_i(h)\right) C_i}{Q_0} h \\
& + p_v h + p_0 \sum_{i=1}^{N_z} \frac{\mu\Big(C_i, I_i\big(h\big)\Big)}{VN_z} h,
\end{aligned}$$

where (p_{C_i}, p_v) are the costates of (C_i, v), respectively, and p_0 is a real number. Suppose that $h^\star \in L^\infty([0, L]; \mathbb{R})$, $h^\star > 0$, is a maximizer and that $C_i^\star$, $v^\star$ are the corresponding solutions of the problem (P1). Using the weak maximum principle [35, pp. 33–35], there exist absolutely continuous functions $p_{C_i}^\star : [0, L] \to \mathbb{R}$, $p_v^\star : [0, L] \to \mathbb{R}$ and a real number $p_0^\star \leq 0$ such that for almost every $x \in [0, L]$, the extremals $(C_i^\star, v^\star, p_{C_i}^\star, p_v^\star, p_0^\star, h^\star)$ satisfy the optimality system

(3.4)

$$C_i' = \frac{\partial H}{\partial p_{C_i}} = \frac{\beta\left(I_i(h)\right) - \alpha\left(I_i(h)\right) C_i}{Q_0} h, \quad v' = \frac{\partial H}{\partial p_v} = h,$$

$$p_{C_i}{}' = -\frac{\partial H}{\partial C_i} = p_{C_i} \frac{\alpha\left(I_i(h)\right)}{Q_0} h + p_0 \frac{\gamma\left(I_i(h)\right)}{V N_z} h, \quad p_v{}' = -\frac{\partial H}{\partial v} = 0,$$

$$0 = \frac{\partial H}{\partial h} = \sum_{i=1}^{N_z} p_{C_i} \frac{\beta'\left(I_i(h)\right) - \alpha'\left(I_i(h)\right) C_i}{Q_0} I_i'(h) h + \sum_{i=1}^{N_z} p_{C_i} \frac{\beta\left(I_i(h)\right) - \alpha\left(I_i(h)\right) C_i}{Q_0}$$
$$+ p_0 \sum_{i=1}^{N_z} \frac{\zeta'\left(I_i(h)\right) - \gamma'\left(I_i(h)\right) C_i}{V N_z} I_i'(h) h + p_0 \sum_{i=1}^{N_z} \frac{\zeta\left(I_i(h)\right) - \gamma\left(I_i(h)\right) C_i}{V N_z} + p_v.$$

LEMMA 3.2. *The extremal* $(C_i^\star, v^\star, p_{C_i}^\star, p_v^\star, p_0^\star, h^\star)$ *that satisfies* (3.4) *is normal.*

Proof. We use the equivalent dual form of the Mangasarian–Fromovitz constraint qualification [33, pp. 255–269]; i.e., we prove that if $p_0^\star = 0$, then $p_{C_i}^\star$ and $p_v^\star$ are equal to zero on $[0, L]$.

Substituting $p_0^\star = 0$ into (3.4), the ODE associated with $p_{C_i}^\star$ then reads as

$$(p_{C_i}^\star)' = p_{C_i}^\star \frac{\alpha\left(I_i(h^\star)\right)}{Q_0} h^\star, \quad p_{C_i}^\star(0) = p_{C_i}^\star(L) \quad \forall i = 1, \cdots, N_z, \tag{3.5}$$

where we complete by the periodic condition determined using $C_i^\star(0) = C_i^\star(L)$ $\forall i = 1, \cdots, N_z$. Note that $Q_0 > 0$, α is a positive function from (2.11), and $h^\star > 0$. Hence, we have $\frac{\alpha(I_i(h^\star))}{Q_0} h^\star > 0$. Using then a similar reasoning to that for the system (2.13), we find that the only solution of (3.5) is $p_{C_i}^\star = 0$. Substituting $p_{C_i}^\star = 0$ and $p_0^\star = 0$ into the last equation of (3.4), we obtain $p_v^\star = 0$, which contradicts the fact that $p_{C_i}^\star$ and $p_v^\star$ are not identically 0 on $[0, L]$. Therefore, $p_0^\star < 0$. ∎

When the extremum is normal, $p_{C_i}^\star$ and $p_v^\star$ are usually normalized so that $p_0^\star = -1$ is what we set hereafter. Let us show that the flat topography satisfies (3.4).

THEOREM 3.3. *There exists* $p_v^f \in \mathbb{R}$ *such that the constant water depth*

$$h^f := \frac{V}{L}$$

and the corresponding solutions $(C_i^f)_{i=1,\cdots,N_z}, (p_{C_i}^f)_{i=1,\cdots,N_z}$, v^f *satisfy* (3.4).

Proof. From $v' = h^f$ with $v(0) = 0$, $v(L) = V$, we find $v^f = \frac{V}{L} x$. Given $i \in \{1, \cdots, N_z\}$, from (3.2), we deduce that

$$I_i(h^f) = I_s \exp\left(-\varepsilon \frac{i - \frac{1}{2}}{N_z} h^f\right), \quad I_i'(h^f) = -\varepsilon \frac{i - \frac{1}{2}}{N_z} I_i(h^f),$$

which are constant on $[0, L]$. Solving the equation of C_i in (3.4) gives

$$C_i(x) = e^{-\frac{\alpha(I_i(h^f))}{Q_0} h^f x} C_i(0) + \frac{\beta(I_i(h^f))}{\alpha(I_i(h^f))} \left(1 - e^{-\frac{\alpha(I_i(h^f))}{Q_0} h^f x}\right). \tag{3.6}$$

Since C_i is periodic (i.e., $C_i(L) = C_i(0)$), we get from the previous equation that $C_i(0) = \frac{\beta(I_i(h^f))}{\alpha(I_i(h^f))}$. Inserting this value into (3.6), we find

$$C_i(x) = C_i^f := \frac{\beta(I_i(h^f))}{\alpha(I_i(h^f))} \quad \forall x \in [0, L].$$

A similar reasoning applied to p_{C_i} gives $p_{C_i}(x) = p^f_{C_i} = \frac{Q_0\gamma(I_i(h^f))}{VN_z\alpha(I_i(h^f))}$ $\forall x \in [0, L]$. It follows that all the terms in the sums of the last equation in (3.4) are constant on $[0, L]$. Hence, there exists a $p^f_v \in \mathbb{R}$ such that the extremal $(C^f_i, v^f, p^f_{C_i}, p^f_v, h^f)$ satisfies the optimality system (3.4). ∎

Remark 3.4. The previous theorem shows that the flat topography satisfies the necessary conditions of optimality. One can further explore second-order conditions to check whether the flat topography is a local maximizer. However, the sign of the eigenvalues of the Hessian operator of the average growth rate $\mathrm{Hess}(\bar{\mu}_{N_z})$ is in general not constant with respect to a flat topography $h^f = V/L$ and is rather difficult to determine (see Appendix B).

Numerically, we observe that the flat topography is actually optimal in the periodic case for standard values of the parameters (see subsection 4.3.4).

Remark 3.5. If C is defined by a Cauchy problem and is not assumed to be periodic (i.e., $C(0)$ is not necessarily equal to $C(L)$), then (3.6) implies that C may depend on x, and the computations in the proof above no longer hold. In other words, the flat topography is not necessarily an optimum in a nonperiodic setting, which is confirmed by our numerical tests (see subsection 4.3.2).

3.3. Nonconstant volume problem for maximizing areal productivity. In the general case, the volume of the system V can also vary and hence can be optimized. We now assume that the water depth is of the form $h + h_0$, where $h \in L^\infty([0, L]; \mathbb{R})$ with $h > -h_0$, $\int_0^L h\,\mathrm{d}x = 0$, and $h_0 > 0$ so that $V = h_0 L$. Here, V depends only on the parameter h_0, as the length $L > 0$ is fixed. Moreover, we have $\frac{1}{L}\int_0^L h + h_0\,\mathrm{d}x = \frac{0+h_0 L}{L} = h_0$, meaning that h_0 represents the average depth of the system.

On the other hand, when V changes, the biomass concentration X (defined by $\dot{X} = (\bar{\mu} - D)X$ with D the dilution rate) also changes. In this case, the light extinction ε in (2.16) can no longer be assumed to be constant. More precisely, we consider here

$$\varepsilon(X) := \varepsilon_0 X + \varepsilon_1, \tag{3.7}$$

where $\varepsilon_0 > 0$ is the specific light extinction coefficient of the microalgae species and $\varepsilon_1 > 0$ stands for the background turbidity that summarizes the light absorption and diffusion caused by all non-microalgae components [22].

To take into account the variation in X with respect to V, we also need to adapt our objective function. More precisely, instead of considering the average net growth rate $\bar{\mu}$, we maximize the areal productivity Π. Given a biomass concentration X, this quantity is defined by

$$\Pi := \bar{\mu} X \frac{V}{S}, \tag{3.8}$$

where $\bar{\mu}$ is the average net growth rate defined in (2.17) and S is the ground surface of the raceway system, which, in our one-dimensional system, actually means $S = L$.

Before stating the associated optimal control problem, we detail the relation between X and V. A standard criterion to determine this relation (see [23, 17]) consists in regulating X such that the steady-state value of the net growth rate μ_s at the average depth h_0 is 0, i.e.,

$$\mu_s\big(I(h_0)\big) = 0, \text{ with } \mu_s(I) := -\gamma(I)\frac{\beta(I)}{\alpha(I)} + \zeta(I). \tag{3.9}$$

Using the definitions (2.11) and (2.15) for α, β, ζ, and γ, one can solve (3.9) analytically and find that $I(h_0)$ is one of the two roots, denoted by I_- and I_+, of the second-order polynomial equation $k_d\tau R(\sigma I)^2 + (k_r\tau\sigma R - k_r k\sigma)I + k_r R = 0$.

In practice, I_-, I_+ are two real roots with $I_- \le I_+$, and $\mu_s(I) \ge 0$ on the interval $[I_-, I_+]$. Then the biomass concentration X in a given volume V is adjusted to get $I(h_0) = I_-$. More precisely, using (2.16) with $I(x,z) = I_-$, we get

$$X(h_0) = \frac{1}{\varepsilon_0}\left(\frac{Y_{\text{opt}}}{h_0} - \varepsilon_1\right), \quad \text{with} \quad Y_{\text{opt}} := \ln\left(\frac{I_s}{I_-}\right). \tag{3.10}$$

Here, X is a function of h_0, meaning that we can use the average depth h_0 to control both V and X in the nonconstant volume case.

Remark 3.6. In bioengineering, the assumption (3.9) is usually called the *compensation condition,* which describes the situation where the growth at the bottom compensates exactly for the respiration. We refer the reader to [2] for a detailed analysis.

We keep using a uniform vertical discretization, as in section 3.1, but now $z_i(0) := \eta(0) - \frac{i-\frac{1}{2}}{N_z}(h_0 + h(0))$, $i = 1, \dots, N_z$. Then the growth rate $\bar{\mu}_{N_z}$ becomes

$$\bar{\mu}_{N_z}(h, h_0) := \sum_{i=1}^{N_z} \int_0^L \frac{\mu\Big(C_i(x), I_i\big(h_0 + h(x)\big)\Big)}{h_0 L N_z}(h_0 + h(x))\,\mathrm{d}x. \tag{3.11}$$

Using (3.10) and (3.11), we then derive the semidiscrete areal productivity from (3.8). Note that $V = h_0 L$, $X(h_0)$, and $\bar{\mu}_{N_z}(h, h_0)$ explicitly depend on the average depth $h_0 > 0$. To treat this parameter, we introduce an additional state variable y such that $y' = 0$ and $y = h_0$. This state variable plays the role of h_0.

We are now in a position to state the optimal control problem. In the nonconstant volume case, we are looking for admissible controls $h \in L^\infty([0, L]; \mathbb{R})$, $h > -y$, and $y > 0$ over a fixed length $L > 0$ which maximize the semidiscrete areal productivity. In view of (3.8), the optimal control problem reads as

$$\max_{\substack{h \in L^\infty([0,L];\mathbb{R}) \\ h > -y,\ y > 0}} \Pi_{N_z}(h) := \sum_{i=1}^{N_z} \int_0^L \frac{\mu\Big(C_i, I_i\big(y + h\big)\Big)}{L N_z}(y + h) X(y)\mathrm{d}x,$$

$$\begin{aligned} C_i' &= \frac{\beta(I_i(h+y)) - \alpha(I_i(h+y))C_i}{Q_0}(h+y), \\ C_i(0) &= C_i(L) \qquad \forall i = 1, \cdots, N_z, \\ v' &= h, \\ v(0) &= 0,\ v(L) = 0, \\ y' &= 0. \end{aligned} \tag{P2}$$

Here again, we use formula (2.14) for μ, and h is the control variable. Moreover, (C_i, v, y) are the state variables, and X is given by (3.10). The Hamiltonian denoted by $\widetilde{H}$ for the optimal control problem (P2) is given by

$$\widetilde{H}(C_i,v,y,p_{C_i},p_v,p_y,p_0,h)=\sum_{i=1}^{N_z}p_{C_i}\frac{\beta(I_i(h+y))-\alpha(I_i(h+y))C_i}{Q_0}(h+y)$$
$$+p_vh+p_y\cdot 0+p_0\sum_{i=1}^{N_z}\frac{\mu\Big(C_i,I_i\big(y+h\big)\Big)}{LN_z}(h+y)X(y).$$

Here, (p_{C_i},p_v,p_y) denote the costates of (C_i,v,y), respectively, and p_0 is a real number. Suppose that $h^\star\in L^\infty([0,L];R)$, $h^\star>-y^\star$, is a maximizer and that $(C_i^\star,v^\star,y^\star)$ are the corresponding solutions of the problem (P2). Using once again the weak maximum principle, there exist absolutely continuous functions $p_{C_i}^\star:[0,L]\to\mathbb{R}$, $p_v^\star:[0,L]\to\mathbb{R}$, $p_y^\star:[0,L]\to\mathbb{R}$ and a real number $p_0^\star\le 0$ such that for almost every $x\in[0,L]$, the extremals $(C_i^\star,v^\star,y^\star,p_{C_i}^\star,p_v^\star,p_y^\star,p_0^\star,h^\star)$ satisfy the optimality system

$$\begin{aligned}
v'&=\frac{\partial\widetilde{H}}{\partial p_v}=h,\quad {p_v}'=-\frac{\partial\widetilde{H}}{\partial v}=0,\quad y'=\frac{\partial\widetilde{H}}{\partial p_y}=0,\\
{p_{C_i}}'&=-\frac{\partial\widetilde{H}}{\partial C_i}=p_{C_i}\frac{\alpha\left(I_i(h+y)\right)}{Q_0}(h+y)+p_0\frac{\gamma\left(I_i(h+y)\right)}{LN_z}(h+y)X(y),\\
C_i'&=\frac{\partial\widetilde{H}}{\partial p_{C_i}}=\frac{\beta\left(I_i(h+y)\right)-\alpha\left(I_i(h+y)\right)C_i}{Q_0}(h+y),\\
{p_y}'&=-\frac{\partial\widetilde{H}}{\partial y}=-\sum_{i=1}^{N_z}p_{C_i}\frac{\beta'\left(I_i(h+y)\right)-\alpha'\left(I_i(h+y)\right)C_i}{Q_0}(h+y)\partial_yI_i(h+y)\\
&\quad-\sum_{i=1}^{N_z}p_{C_i}\frac{\beta\left(I_i(h+y)\right)-\alpha\left(I_i(h+y)\right)C_i}{Q_0}\\
&\quad-p_0\sum_{i=1}^{N_z}\frac{\zeta'\left(I_i(h+y)\right)-\gamma'\left(I_i(h+y)\right)C_i}{LN_z}(h+y)X(y)\partial_yI_i(h+y)\\
&\quad-p_0\sum_{i=1}^{N_z}\frac{\zeta\left(I_i(h+y)\right)-\gamma\left(I_i(h+y)\right)C_i}{LN_z}\big(X(y)+(h+y)X'(y)\big)-p_v,\\
0&=\frac{\partial\widetilde{H}}{\partial h}=\sum_{i=1}^{N_z}p_{C_i}\frac{\beta'\left(I_i(h+y)\right)-\alpha'\left(I_i(h+y)\right)C_i}{Q_0}(h+y)\partial_hI_i(h+y)\\
&\quad+\sum_{i=1}^{N_z}p_{C_i}\frac{\beta\left(I_i(h+y)\right)-\alpha\left(I_i(h+y)\right)C_i}{Q_0}\\
&\quad+p_0\sum_{i=1}^{N_z}\frac{\zeta'\left(I_i(h+y)\right)-\gamma'\left(I_i(h+y)\right)C_i}{LN_z}(h+y)X(y)\partial_hI_i(h+y)\\
&\quad+p_0\sum_{i=1}^{N_z}\frac{\zeta\left(I_i(h+y)\right)-\gamma\left(I_i(h+y)\right)C_i}{LN_z}X(y)+p_v.
\end{aligned}\tag{3.12}$$

LEMMA 3.7. *The extremals $(C_i^\star,v^\star,y^\star,p_{C_i}^\star,p_v^\star,p_y^\star,p_0^\star,h^\star)$, which satisfy* (3.12)*, are normal.*

Proof. We follow the same reasoning as in the proof of Lemma 3.2. Suppose that $p_0^\star=0$, and substitute it into the system (3.12). The ODE associated with $p_{C_i}^\star$ becomes

$$p_{C_i}{}' = p_{C_i}\frac{\alpha\left(I_i(h^\star+y^\star)\right)}{Q_0}(h^\star+y^\star), \quad p^\star_{C_i}(0) = p^\star_{C_i}(L) \quad \forall i = 1,\cdots,N_z.$$

Since $y^\star = h_0 > 0$ and the function $h^\star > y^\star$, we have $\frac{\alpha(I_i(h^\star+y^\star))}{Q_0}(h^\star+y^\star) > 0$. This implies that $p^\star_{C_i} = 0$. Substituting then $p^\star_{C_i} = 0$ and $p^\star_0 = 0$ into the last equation in the system (3.12), we obtain that $p^\star_v = 0$, which then implies that $p^{\star\prime}_y = 0$. As p_y is the costate associated with the constant $y = h_0$, we have $p^\star_y(0) = p^\star_y(L) = 0$, meaning that $p^\star_y$ also constantly equals 0. Thus, $p^\star_{C_i}$, $p^\star_v$, $p^\star_y$ are identically 0 on $[0, L]$, which concludes the proof. ∎

Based on Lemma 3.7, we can normalize the costates such that $p_0 = -1$. However, unlike Theorem 3.3, the flat topography does not satisfy the optimality system (3.12).

THEOREM 3.8. *Given $h_0 > 0$, let $h^f := 0$, $y^f := h_0$, $p_0 = -1$, and assume that $I_s \in (I_-, I_+)$. Then there does not exist a triple (C_i^f, p_y^f, p_v^f) that satisfies the last three equations in the optimality system* (3.12).

Proof. Assuming that there exists such a triple, we start by solving the ODE associated with C_i^f in (3.12). From (3.2), (3.7), and (3.10), we obtain

$$I_i(h+y) = I_s \exp\left(-\frac{Y_{\text{opt}}}{y}\frac{i-\frac{1}{2}}{N_z}(h+y)\right), \tag{3.13}$$

where Y_{opt} is defined in (3.10). Substituting the values of h^f and y^f into (3.13), we find that $I_i(h^f + y^f) = I_i(h_0) = I_s \exp(-Y_{\text{opt}}\frac{i-\frac{1}{2}}{N_z})$, which is a constant with respect to h_0. A similar analysis to that of the proof of Theorem 3.3 shows that $C_i^f = \beta(I_i(h_0))/\alpha(I_i(h_0))$, which is also a constant. Furthermore, differentiating $I_i(h+y)$ with respect to y gives $\partial_y I_i(h+y) = I_i(h+y)\cdot\frac{Y_{\text{opt}}}{y^2}\cdot\frac{i-\frac{1}{2}}{N_z}h$. Setting $h = h^f$ in this expression, we get $\partial_y I_i(h^f + y) = \partial_y I_i(0+y) = 0$. Substituting all these expressions into the last two equations in (3.12), we get

$$(p_y^f)' = \frac{X(h_0) + h_0 X'(h_0)}{LN_z}\sum_{i=1}^{N_z}\mu_s\big(I_i(h_0)\big) - p_v^f, \quad p_v^f = \frac{X(h_0)}{LN_z}\sum_{i=1}^{N_z}\mu_s\big(I_i(h_0)\big).$$

This implies that $(p_y^f)' = -\frac{Y_{\text{opt}}}{LN_z h_0 \varepsilon_0}\sum_{i=1}^{N_z}\mu_s\big(I_i(h_0)\big)$ so that using (3.10), we get $X'(h_0) = -\frac{Y_{\text{opt}}}{h_0^2\varepsilon_0}$. Moreover, $I_i(h_0) \in [I_{N_z}(h_0), I_1(h_0)] \subset (I_-, I_s) \subset (I_-, I_+)$; hence, $\mu_s(I_i(h_0)) > 0$ for $i \in \{1,\cdots,N_z\}$. We deduce that $(p_y^f)' < 0$. As $p_y^f(0) = p_y^f(L) = 0$, we find a contradiction, which concludes the proof. ∎

Remark 3.9. Note that the coefficient h_0 considered in Theorem 3.8 must satisfy $h_c \le h_0$ to guarantee that the system remains in a subcritical regime (see Remark 2.1).

4. Numerical experiments. In this section, we show some optimal topographies obtained in the various previous frameworks.

4.1. Numerical methods. To solve our optimization problem numerically, we introduce a supplementary space discretization with respect to x. In this way, let us take a space increment Δx and set $N_x = [L/\Delta x]$ and $x^{n_x} = n_x\Delta x$ for $n_x = 0,\ldots,N_x$. We use Heun's method to compute $(C_i)_{i=1}^{N_z}$ via (3.4). Following a first-discretize-then-optimize strategy, we get that the costates $(p_i^C)_{i=1}^{N_z}$ are also computed by a Heun-type scheme. Note that this scheme is still explicit since it solves a backward dynamics starting from $p_i(L) = 0$. The optimization is then achieved by a standard gradient method using (3.4) and (3.12), where the stopping criterion involves both the

TABLE 4.1
Parameter values for the Han model.

k_r	$6.8\ 10^{-3}$	s^{-1}
k_d	$2.99\ 10^{-4}$	–
τ	0.25	s
σ	0.047	$\mathrm{m}^2\mu\mathrm{mol}^{-1}$
k	$8.7\ 10^{-6}$	–
R	$1.389\ 10^{-7}$	s^{-1}

magnitude of the gradient and the constraint $h \geq h_c$; see Remark 2.1. The numerical tests are performed by MATLAB R2020a [34].

4.2. Parameter setting. We now detail the parameters used in our simulations.

4.2.1. Parameterization. In our tests, we parameterize h using a truncated Fourier series. More precisely, the water depth reads as

$$h(x;\boldsymbol{a}) + h_0 = h_0 + \sum_{n=1}^{N} a_n \sin\left(2n\pi\frac{x}{L}\right),$$

with $\boldsymbol{a} = (a_1, \ldots, a_N)$. This parameterization is motivated by three reasons:

- The regularity of the topography is controlled by the order of truncation N. As an example, limit situations where $N \to +\infty$ are not considered in what follows. This framework is consistent with the hydrodynamic regime under consideration, where the solutions of the Saint-Venant equations are smooth.
- The constraint $h(0;\boldsymbol{a}) = h(L;\boldsymbol{a})$ is preserved, which fits the toric shape of the raceway pond.
- The water depth has the form $h_0 + h$, as assumed in section 3.3.

From (2.2) and (2.4), u and z_b also read as functions of $\boldsymbol{a}$. Once the vector $\boldsymbol{a}$ that maximizes $\bar{\mu}_{N_z}$ is determined, we then find the optimal topography of our system.

4.2.2. Parameter for the models. The spatial increment is set to $\Delta x = 0.01\,\mathrm{m}$ so that the convergence of the numerical scheme has been ensured, and we set $L = 100\,\mathrm{m}$, $Q_0 = 0.04\,\mathrm{m}^2\,\mathrm{s}^{-1}$, and the average depths (in the constant volume case) $h_0 = h(0;\boldsymbol{a}) = 0.4\,\mathrm{m}$ and $z_b(0) = -0.4\,\mathrm{m}$ to stay in standard ranges for a raceway [14]. The free fall acceleration $g = 9.81\,\mathrm{m\,s}^{-2}$. The values of all parameters in the Han model are taken from [16] and given in Table 4.1.

In order to determinate the light extinction ε, two cases must be considered:

- Constant volume: We assume that only 1% of light can be captured by the cells at the average depth of the raceway, meaning that $I_- = 0.01 I_s$. We choose $I_s = 2000\,\mu\mathrm{mol\,m}^{-2}\,\mathrm{s}^{-1}$, which approximates the maximum light intensity, e.g., in summer in the south of France. Then ε can be computed by $\varepsilon = (1/h_0)\ln(I_s/I_-)$.
- Nonconstant volume: In this case, h_0 is also a parameter to be optimized. We take from [22] the specific light extinction coefficient of microalgae species $\varepsilon_0 = 0.2\,\mathrm{m}^2 \cdot \mathrm{g}$ and the background turbidity $\varepsilon_1 = 10\,\mathrm{m}^{-1}$.

4.3. Numerical results. We test the influence of various parameters on optimal topographies. In all of our experiments, we always observe that the obtained topographies satisfy $\min_{x\in[0,L]} h(x;\boldsymbol{a}) > h_c$.

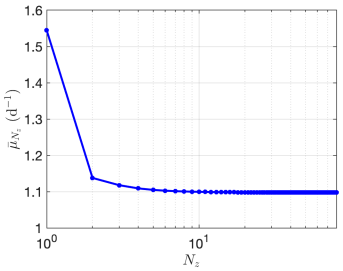

FIG. 4.1. *Values of the functional* $\bar{\mu}_{N_z}$ *for* $N_z = [1, 80]$.

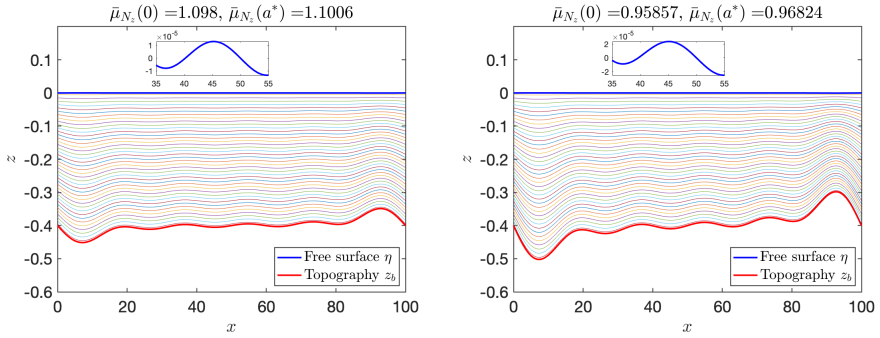

FIG. 4.2. *Optimal topography for* $C_0 = 0.1$ *(left) and* $C_0 = 0.9$ *(right). The red thick line represents the topography* z_b*, the blue thick line represents the free surface* η*, and all the other curves in between represent the different trajectories.* $\bar{\mu}_{N_z}(0)$*: flat topography;* $\bar{\mu}_{N_z}(\boldsymbol{a}^*)$*: optimal topography.*

4.3.1. Influence of vertical discretization. The first test consists of studying the influence of the vertical discretization parameter N_z. We choose $N = 5$, $C_0 = 0.1$ and consider 100 random values a. Note that the choice of a should respect the subcritical condition. Let N_z vary from 1 to 80, and we compute the average value of $\bar{\mu}_{N_z}$ for each N_z. The results are shown in Figure 4.1. We observe numerical convergence when N_z grows, showing the convergence toward the continuous model in space. In view of these results, we take hereafter $N_z = 40$.

4.3.2. Influence of the initial condition. Here, we study the influence of the initial condition C_0 on the optimal shape of the raceway pond. We set the numerical tolerance to Tol$= 10^{-10}$ and consider the order of truncation $N = 5$. As for the initial guess, we consider the flat topography, meaning that $\boldsymbol{a}$ is set to 0. We compare the optimal topographies obtained with $C_0 = 0.1$ and $C_0 = 0.9$. The result is shown in Figure 4.2. This test confirms Remark 3.5 since we obtain nontrivial topographies which slightly enhance the algal average growth rate. Moreover, a slight difference between the two optimal topographies is observed. We have observed that this difference remains when the spatial increment Δx goes to zero. Although it is difficult to observe in Figure 4.2, the free surface is not equal to zero, as can be seen for $x \in [35, 55]$.

4.3.3. Influence of Fourier series truncation. The next test is dedicated to the study of the influence of the order of truncation N used to parameterize the water depth h. Set $N = [0, 5, 10, 15, 20]$, $C_0 = 0.1$, and keep all the other parameters

TABLE 4.2
Behavior of the objective function for various orders of truncation N.

N	Iteration	$\bar{\mu}_{N_z}(\boldsymbol{a}^*)(\mathrm{d}^{-1})$	$\log_{10}(\|\nabla\bar{\mu}_{N_z}(\boldsymbol{a}^*)\|)$	$\lambda_{max}(\text{Hess }\bar{\mu}_{N_z}(\boldsymbol{a}^*))$
0	0	1.098	–	–
5	16	1.1006	-10.208017	-6.1400
10	17	1.1013	-10.240885	-5.9141
15	17	1.1016	-10.258798	-5.9074
20	18	1.1018	-10.269413	-5.9032

as in the previous section. Table 4.2 shows the optimal values of $\bar{\mu}_{N_z}(\boldsymbol{a}^*)$ and the corresponding maximum eigenvalues of the Hessian $\lambda_{max}(\text{Hess }\bar{\mu}_{N_z}(\boldsymbol{a}^*))$ for various values of N. The result shows a slight increase in the optimal value of $\bar{\mu}_{N_z}(\boldsymbol{a}^*)$ when N becomes larger. However, the corresponding values of $\bar{\mu}_{N_z}(\boldsymbol{a}^*)$ remain close to the one associated with a flat topography. Furthermore, the maximum spectrum $\lambda_{max}(\text{Hess }\bar{\mu}_{N_z}(\boldsymbol{a}^*))$ is always negative, which confirms that local maximizers are obtained.

4.3.4. Optimal topographies in the periodic case. We study the optimal topographies in the constant volume case where the photoinhibition state C is periodic. In our discrete setting, the Hessian operator is actually of the form $\text{Hess }\bar{\mu}_{N_z}(h^f) = \lambda Id_N$ with Id_N the identity matrix of size N. We observe that $\lambda < 0$, which confirms that the flat topography is a local maximizer. A precise computation of λ together with some remarks about its sign can be found in Appendix B.

In order to test whether this local maximizer is global, we run the optimization procedure with random admissible topographies. We observe that the procedure always converges to a flat topography (i.e., $\boldsymbol{a}^* = a_f$). This leads us to conjecture that the flat topography corresponds to the global maximum for the average growth rate. For the variable volume case, let us set $N = 5$ (i.e., $\tilde{\boldsymbol{a}} \in \mathbb{R}^6$) and $h_0 = 0.4$ as an initial guess of the average depth. We observe that the optimization stops due to the presence of the physical constraint h_c. However, a smaller depth increases the areal productivity, in some cases more than twice the initial areal productivity.

4.3.5. Simulation with a paddle wheel. In this paragraph, we consider the full raceway pond, where the mixing induced by the paddle wheel is also considered. More precisely, we simulate several laps with a paddle wheel that mixes up the algae after each lap. The turbulent mixing of the paddle wheel is modeled by a permutation matrix P, which rearranges the trajectories in each lap. In our test, P is chosen as an antidiagonal matrix with entries equal to one. This choice actually corresponds to an optimum, as shown in [4], where other choices are also investigated.

The permutation matrix P corresponds to the permutation $\pi = (1\ N_z)(2\ N_z - 1)(3\ N_z - 2)\ldots$, where we use the standard notation of cycles in the symmetric group. Note that π is of order two. The photoinhibition state C is then set to be 2-periodic (i.e., $C^1(0) = PC^2(L)$, where C^1 and C^2 correspond to the photoinhibition state during the first and the second lap, respectively). The details of the optimization procedure are given in Appendix A.

We choose a truncation of order $N = 5$ in the Fourier series. The initial guess a is set to zero. Figure 4.3 presents the shape of the optimal topography and the evolution of the photoinhibition state C over two laps. The resulting optimal topography in this case is not flat. However, the increases in the optimal value of the objective function $\bar{\mu}_{N_z}$ compared to a flat topography with and without permutation are 0.217% and

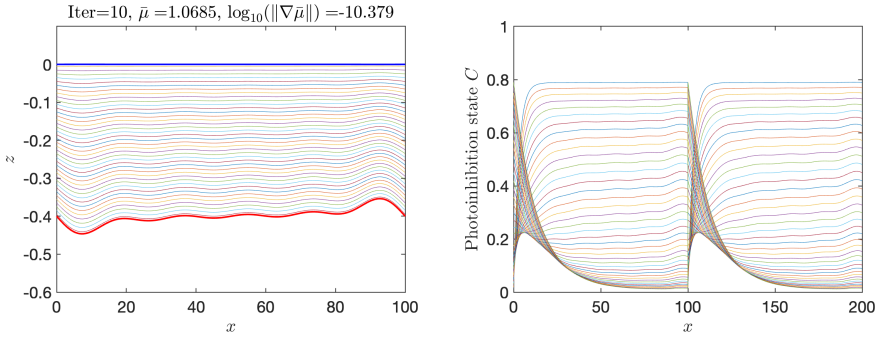

FIG. 4.3. *Optimal topography (left) and evolution of the photoinhibition state C (right) over two laps.*

0.265%, respectively, meaning that the increases remain small. On the other hand, we observe that the state C is actually periodic for each lap. This result is actually proved for an arbitrary P in [4] in the case of a flat topography. This justifies that the optimization strategy only needs to focus on one lap of the raceway (whatever the permutation) and leaves the door open to the optimization of such mixing strategies. We refer the reader to [3, 5] for more details on optimal mixing strategies.

5. Conclusions and future works. A flat topography cancels the average algal growth rate gradient when C is assumed to be periodic along the laminar parts of the raceway. This is further confirmed by our numerical tests, in which maximum productivity is obtained for a flat topography. However, considering a more complete framework without periodicity and including a mixing device gives rise to an optimal nonflat topography with a slight gain of the average growth rate. It is not clear whether the difficulty in designing such a pattern could be compensated for by the increase in the process productivity.

These results may no longer hold if the hydrodynamic regime is turbulent along the entire raceway. In such a case, the increase in the algal productivity may compensate for the higher energetic cost of mixing. However, without the laminar assumption, the problem becomes challenging, and much work remains to be done in this direction.

Appendix A. Two-lap system with a paddle wheel. Denote by P the permutation matrix associated with $\pi = (1\ N_z)(2\ N_z-1)(3\ N_z-2)\dots$ (see section 4.3.5), i.e., 1 as entries on the antidiagonal, and by C^1 (resp., C^2) the photoinhibition state for the first (resp., second) lap of the raceway. We then assume that the state C is 2-periodic, meaning that $C^1(0) = PC^2(L)$. From (3.3), we define the objective function by

$$\frac{1}{2}\sum_{j=1}^{2}\bar{\mu}^j_{N_z}(h) = \frac{1}{2}\sum_{j=1}^{2}\sum_{i=1}^{N_z}\int_0^L \frac{\mu\Big(C_i^j(x), I_i\big(h(x)\big)\Big)}{VN_z}h\,\mathrm{d}x.$$

For a fixed volume $V > 0$ and a discharge $Q_0 > 0$, the associated optimal control problem reads as

$$\max_{h\in L^\infty(0,L;\mathbb{R}),\ h>0} \frac{1}{2}\sum_{j=1}^{2}\bar{\mu}_{N_z}(h) = \frac{1}{2}\sum_{j=1}^{2}\sum_{i=1}^{N_z}\int_0^L \frac{\mu\Big(C_i^j(x), I_i\big(h(x)\big)\Big)}{VN_z}h\,\mathrm{d}x,$$

$$\begin{aligned} C_i^{j\prime} &= \frac{\beta\left(I_i(h)\right) - \alpha\left(I_i(h)\right)C_i^j}{Q_0}h, \\ C^1(L) &= PC^2(0), \quad C^1(0) = PC^2(L), \\ v' &= h, \\ v(0) &= 0,\ v(L) = V. \end{aligned} \tag{A.1}$$

Denote by H the Hamiltonian associated with this problem, which reads as

$$\begin{aligned} H(C_i^j, v, p_{C_i}^j, p_v, p_0, h) = &\sum_{j=1}^{2}\sum_{i=1}^{N_z} p_{C_i}^j\Big(\frac{\beta\left(I_i(h)\right) - \alpha(I_i(h))C_i^j}{Q_0}h\Big) + p_v h \\ &+ p_0\frac{1}{2}\sum_{j=1}^{2}\sum_{i=1}^{N_z}\frac{\zeta\left(I_i(h)\right) - \gamma\left(I_i(h)\right)C_i^j}{VN_z}h, \end{aligned}$$

where $p_{C_i}^j$, p_v are the costates of C_i, v and p_0 is a real number. A similar analysis to that of section 3.2 gives a similar optimality system as (3.4), in which $p_{C_i}^j$ satisfies the conditions $p_C^1(L) = Pp_C^2(0)$ and $p_C^2(L) = Pp_C^1(0)$.

Appendix B. Second-order conditions. Consider the second-order condition under the truncated Fourier parameterization. Since Fourier modes $(\sin(2n\pi\frac{x}{L}))_{n\in\mathbb{N}}$ are orthogonal, a direct computation gives Hess $\bar{\mu}_{N_z}(h^f) = \lambda Id_N$ with

$$\begin{aligned} \lambda = &\frac{1}{Q_0}\sum_{i=1}^{N_z} 2p_{C_i}\big(\beta'(I_i(h)) - \alpha'(I_i(h))C_i\big)I_i'(h) + p_{C_i}\big(\beta'(I_i(h)) - \alpha'(I_i(h))C_i\big)I_i''(h)h \\ &+ p_{C_i}\big(\beta''(I_i(h)) - \alpha''(I_i(h))C_i\big)I_i'(h)^2 h \\ &+ \frac{p_0}{VN_z}\sum_{i=1}^{N_z} 2\big(\zeta'(I_i(h)) - \gamma'(I_i(h))C_i\big)I_i'(h) + \big(\zeta'(I_i(h)) - \gamma'(I_i(h))C_i\big)I_i''(h)h \\ &+ \big(\zeta''(I_i(h)) - \gamma''(I_i(h))C_i\big)I_i'(h)^2 h. \end{aligned}$$

Using the definitions (2.11) and (2.15), we get $\alpha(I) = \beta(I) + k_r$ and $\zeta(I) = \gamma(I) - R$. As $\alpha'(I) = \beta'(I)$ and $\zeta'(I) = \gamma'(I)$, one gets

$$\begin{aligned} \lambda = \sum_{i=1}^{N_z}(1 - C_i)\Bigg[&\frac{p_{C_i}}{Q_0}\Big(2\beta'(I_i(h))I_i'(h) + \beta'(I_i(h))I_i''(h)h + \beta''(I_i(h))I_i'(h)^2 h\Big) \\ &+ \frac{p_0}{VN_z}\Big(2\gamma'(I_i(h))I_i'(h) + \gamma'(I_i(h))I_i''(h)h + \gamma''(I_i(h))I_i'(h)^2 h\Big)\Bigg]. \end{aligned} \tag{B.1}$$

Furthermore, one can differentiate the closed forms of $I(h)$, $\beta(I)$, and $\gamma(I)$ to have

$$\begin{aligned} &I_i'(h) = -\varepsilon\frac{i - \frac{1}{2}}{N_z}I_i(h), \quad I_i''(h) = \left(\varepsilon\frac{i - \frac{1}{2}}{N_z}\right)^2 I_i(h), \\ &\beta''(I) = \frac{2}{(\tau\sigma I + 1)(\tau\sigma I + 2)I}\beta'(I), \quad \gamma''(I) = -\frac{2\sigma\tau}{\tau\sigma I + 1}\gamma'(I). \end{aligned}$$

Inserting these analytical forms into (B.1) gives

$$\lambda = \sum_{i=1}^{N_z} (1-C_i)\varepsilon \frac{i-\frac{1}{2}}{N_z} I_i(h) \left[\frac{p_{C_i}\beta'(I_i(h))}{Q_0} \left(h\varepsilon \frac{i-\frac{1}{2}}{N_z} + \frac{2h\varepsilon \frac{i-\frac{1}{2}}{N_z}}{(\tau\sigma I_i(h)+1)(\tau\sigma I_i(h)+2)} - 2 \right) + \frac{p_0\gamma'(I_i(h))}{VN_z} \left(h\varepsilon \frac{i-\frac{1}{2}}{N_z} - \frac{2\sigma\tau h\varepsilon \frac{i-\frac{1}{2}}{N_z} I_i(h)}{\tau\sigma I_i(h)+1} - 2 \right) \right].$$

Considering now the case $h = h^f = V/L$, one gets

$$1 - C_i^f = \frac{k_r}{\alpha(I_i(h^f))} > 0, \quad p_{C_i}^f = p_0 \frac{Q_0\gamma(I_i(h^f))}{VN_z\alpha(I_i(h^f))} < 0,$$
$$\beta'(I) = \frac{k_d\tau\sigma^2 I(I\sigma\tau+2)}{(I\sigma\tau+1)^2} > 0, \quad \gamma'(I) = \frac{k\sigma}{(I\sigma\tau+1)^2} > 0.$$

Hence, in the limit case, the sign in the big bracket becomes positive when h goes to 0, and the flat topography is no longer a local maximizer for small values of h in this case. Under the assumption that the hydrodynamics is subcritical, $\lambda < 0$ in practice, as shown in sections 4.3.3 and 4.3.4.

Acknowledgments. We are very grateful to Emmanuel Trélat (Laboratoire Jacques-Louis Lions, Sorbonne Université, Paris) for the helpful discussions we have had on this topic. We thank the editors and anonymous referees for their valuable and constructive comments, which greatly improved the quality of this paper.

REFERENCES

[1] O. Bernard, A.-C. Boulanger, M.-O. Bristeau, and J. Sainte-Marie, *A 2D model for hydrodynamics and biology coupling applied to algae growth simulations*, ESAIM Math. Model. Numer. Anal., 47 (2013), pp. 1387–1412, https://doi.org/10.1051/m2an/2013072.

[2] O. Bernard and L.-D. Lu, *Optimal optical conditions for microalgal production in photobioreactors*, J. Process Control, 112 (2022), pp. 69–77, https://doi.org/10.1016/j.jprocont.2022.03.001.

[3] O. Bernard, L.-D. Lu, and J. Salomon, *Mixing strategies combined with shape design to enhance productivity of a raceway pond*, in ADCHEM 2021—16th IFAC Symposium on Advanced Control of Chemical Processes, Vol. 54, Elsevier, New York, 2021, pp. 281–286.

[4] O. Bernard, L.-D. Lu, and J. Salomon, *Optimizing microalgal productivity in raceway ponds through a controlled mixing device*, in 2021 American Control Conference (ACC), IEEE, New York, 2021, pp. 640–645.

[5] O. Bernard, L.-D. Lu, and J. Salomon, *Optimal periodic resource allocation in reactive dynamical systems: Application to microalgal production*, Int. J. Robust Nonlinear Control, 33 (2023), pp. 4989–5010, https://doi.org/10.1002/rnc.6171.

[6] O. Bernard, F. Mairet, and B. Chachuat, *Modelling of microalgae culture systems with applications to control and optimization*, in Microalgae Biotechnology, Springer-Verlag, Berlin, 2015, pp. 59–87, https://doi.org/10.1007/10_2014_287.

[7] A. Bouharguane and B. Mohammadi, *Minimisation principles for the evolution of a soft sea bed interacting with a shallow sea*, Int. J. Comput. Fluid Dyn., 26 (2012), pp. 163–172, https://doi.org/10.1080/10618562.2012.669831.

[8] F. Casagli, G. Zuccaro, O. Bernard, J.-P. Steyer, and E. Ficara, *ALBA: A comprehensive growth model to optimize algae-bacteria wastewater treatment in raceway ponds*, Water Res., 190 (2021), 116734, https://doi.org/10.1016/j.watres.2020.116734.

[9] D. Chiaramonti, M. Prussi, D. Casini, M. Tredici, L. Rodolfi, N. Bassi, G. Zittelli, and P. Bondioli, *Review of energy balance in raceway ponds for microalgae cultivation: Re-thinking a traditional system is possible*, Appl. Energy, 102 (2013), pp. 101–111, https://doi.org/10.1016/j.apenergy.2012.07.040.

[10] P.-H. Cocquet, S. Riffo, and J. Salomon, *Optimization of bathymetry for long waves with small amplitude*, SIAM J. Control Optim., 59 (2021), pp. 4429–4456, https://doi.org/10.1137/20M1326337.

[11] R. De-Luca, F. Bezzo, Q. Béchet, and O. Bernard, *Exploiting meteorological forecasts for the optimal operation of algal ponds*, J. Process Control, 55 (2017), pp. 55–65, https://doi.org/10.1016/j.jprocont.2017.03.010.

[12] D. Demory, C. Combe, P. Hartmann, A. Talec, E. Pruvost, R. Hamouda, F. Souillé, P.-O. Lamare, M.-O. Bristeau, J. Sainte-Marie, S. Rabouille, F. Mairet, A. Sciandra, and O. Bernard, *How do microalgae perceive light in a high-rate pond? Towards more realistic Lagrangian experiments*, R. Soc. Open Sci., 5 (2018), 180523, http://doi.org/10.1098/rsos.180523.

[13] P. Eilers and J. Peeters, *Dynamic behaviour of a model for photosynthesis and photoinhibition*, Ecol. Model., 69 (1993), pp. 113–133, https://doi.org/10.1016/0304-3800(93)90052-T.

[14] T. B. F. Rayen and P. Dominique, *Optimization of a raceway pond system for wastewater treatment: A review*, Crit. Rev. Biotechnol., 39 (2019), pp. 422–435, https://doi.org/10.1080/07388551.2019.1571007.

[15] J.-F. Gerbeau and B. Perthame, *Derivation of viscous Saint-Venant system for laminar shallow water: Numerical validation*, Discrete Contin. Dyn. Syst. B, 1 (2001), pp. 89–102, https://doi.org/10.3934/dcdsb.2001.1.89.

[16] J. Ignacio Fierro Ulloa, L. D. Lu, and O. Bernard, *Theoretical growth rate of microalgae under high/low-flashing light*, J. Math. Biol., 86 (2024), https://doi.org/10.1007/s00285-023-01871-2.

[17] F. Grognard, A. Akhmetzhanov, and O. Bernard, *Optimal strategies for biomass productivity maximization in a photobioreactor using natural light*, Automatica, 50 (2014), pp. 359–368, https://doi.org/10.1016/j.automatica.2013.11.014.

[18] B.-P. Han, *A mechanistic model of algal photoinhibition induced by photodamage to photosystem*-II, J. Theoret. Biol., 214 (2002), pp. 519–527, https://doi.org/10.1006/jtbi.2001.2468.

[19] R. Hreiz, B. Sialve, J. Morchain, R. Escudié, J.-P. Steyer, and P. Guiraud, *Experimental and numerical investigation of hydrodynamics in raceway reactors used for algaculture*, Chem. Eng. J., 250 (2014), pp. 230–239, https://doi.org/10.1016/j.cej.2014.03.027.

[20] C. Inostroza, A. Solimeno, J. García, J. Fernández-Sevilla, and F. Acién, *Improvement of real-scale raceway bioreactors for microalgae production using Computational Fluid Dynamics (CFD)*, Algal Res., 54 (2021), 102207, https://doi.org/10.1016/j.algal.2021.102207.

[21] P.-O. Lamare, N. Aguillon, J. Sainte-Marie, J. Grenier, H. Bonnefond, and O. Bernard, *Gradient-based optimization of a rotating algal biofilm process*, Automatica, 105 (2019), pp. 80–88, https://doi.org/10.1016/j.automatica.2019.02.043.

[22] C. Martínez, F. Mairet, and O. Bernard, *Theory of turbid microalgae cultures*, J. Theoret. Biol., 456 (2018), pp. 190–200, https://doi.org/10.1016/j.jtbi.2018.07.016.

[23] P. Masci, F. Grognard, and O. Bernard, *Microalgal biomass surface productivity optimization based on a photobioreactor model*, IFAC Proc. Vol., 43 (2010), pp. 180–185, https://doi.org/10.3182/20100707-3-BE-2012.0014.

[24] J. Masojídek, Š. Papáček, M. Sergejevová, V. Jirka, J. Červený, J. Kunc, J. Korečko, O. Verbovikova, J. Kopecký, D. Štys, and G. Torzillo, *A closed solar photobioreactor for cultivation of microalgae under supra-high irradiance: Basic design and performance*, J. Appl. Phycol., 15 (2003), pp. 239–248, https://doi.org/10.1023/A:1023849117102.

[25] J. Mendoza, M. Granados, I. De Godos, F. Acién, E. Molina, C. Banks, and S. Heaven, *Fluid-dynamic characterization of real-scale raceway reactors for microalgae production*, Biomass Bioenergy, 54 (2013), pp. 267–275, https://doi.org/10.1016/j.biombioe.2013.03.017.

[26] V. Michel-Dansac, C. Berthon, S. Clain, and F. Foucher, *A well-balanced scheme for the shallow-water equations with topography*, Comput. Math. Appl., 72 (2016), pp. 586–593, https://doi.org/10.1016/j.camwa.2016.05.015.

[27] B. Mohammadi and A. Bouharguane, *Optimal dynamics of soft shapes in shallow waters*, Comput. & Fluids, 40 (2011), pp. 291–298, https://doi.org/10.1016/j.compfluid.2010.09.031.

[28] R. Muñoz-Tamayo, F. Mairet, and O. Bernard, *Optimizing microalgal production in raceway systems*, Biotechnol. Progr., 29 (2013), pp. 543–552, https://doi.org/10.1002/btpr.1699.

[29] G. Olivieri, L. Gargiulo, P. Lettieri, L. Mazzei, P. Salatino, and A. Marzocchella, *Photobioreactors for microalgal cultures: A Lagrangian model coupling hydrodynamics and kinetics*, Biotechnol. Progr., 31 (2015), pp. 1259–1272, https://doi.org/10.1002/btpr.2138.

[30] S. Papacek, J. Jablonsky, and K. Petera, *Advanced integration of fluid dynamics and photosynthetic reaction kinetics for microalgae culture systems*, BMC Syst. Biol., 12 (2018), pp. 1–12, https://doi.org/10.1186/s12918-018-0611-9.
[31] C. Posten and S. Chen, *Microalgae Biotechnology*, Vol. 153, Springer-Verlag, Berlin, 2016.
[32] M. Prussi, M. Buffi, D. Casini, D. Chiaramonti, F. Martelli, M. Carnevale, M. Tredici, and L. Rodolfi, *Experimental and numerical investigations of mixing in raceway ponds for algae cultivation*, Biomass Bioenergy, 67 (2014), pp. 390–400, https://doi.org/10.1016/j.biombioe.2014.05.024.
[33] M. V. Solodov, *Constraint Qualifications*, John Wiley, New York, 2011.
[34] The MathWorks, Inc., *MATLAB Version 9.8.0 (r2020a)*, The MathWorks, Inc., Natick, MA, 2020.
[35] E. Trélat, *Control in Finite and Infinite Dimension*, Springer-Verlag, Berlin, 2024.
[36] A. van Dongeren, N. Plant, A. Cohen, D. Roelvink, M. Haller, and P. Catalán, *Beach Wizard: Nearshore bathymetry estimation through assimilation of model computations and remote observations*, Coast. Eng., 55 (2008), pp. 1016–1027, https://doi.org/10.1016/j.coastaleng.2008.04.011.
[37] R. Wijffels and M. Barbosa, *An outlook on microalgal biofuels*, Science, 329 (2010), pp. 796–799, https://doi.org/10.1126/science.1189003.
[38] S. Yoo, S.-K. Oh, and J. Lee, *Design of experiments and sensitivity analysis for microalgal bioreactor systems*, in 22nd European Symposium on Computer Aided Process Engineering, Computer Aided Chemical Engineering 30, I. D. L. Bogle and M. Fairweather, eds., Elsevier, New York, 2012, pp. 722–726.